Internally-driven inertial waves in geodynamo simulations

Note: The following files were submitted by the author for peer review, but cannot be converted to PDF. You must view these files (e.g. movies) online.

ms01_T_s0.62.gif
ms02_T_s0.99.gif
ms03_T_Eq.gif
ms04_uz_s0.62.gif
ms05_uz_s0.99.gif

Internally-driven inertial waves in geodynamo simulations

A. Ranjan[1], P. A. Davidson[1], U. R. Christensen[2] & J. Wicht[2]

[1] *Department of Engineering, University of Cambridge, UK*

[2] *Max-Planck-Institut für Sonnensystemforschung, Göttingen, Germany*

SUMMARY

Inertial waves are oscillations in a rotating fluid, such as the Earth's outer core, which result from the restoring action of the Coriolis force. In an earlier work, it was argued by Davidson that inertial waves launched near the equatorial regions could be important for the α^2 dynamo mechanism, as they can maintain a helicity distribution which is negative (positive) in the north (south). Here we identify such internally-driven inertial waves, triggered by buoyant anomalies in the equatorial regions in a strongly-forced geodynamo simulation. Using the time-derivative of vertical velocity, $\partial u_z/\partial t$, as a diagnostic for travelling wave-fronts, we find that the horizontal movement in the buoyancy field near the equator is well-correlated with a corresponding movement of the fluid far from the equator. Moreover, the azimuthally-averaged spectrum of $\partial u_z/\partial t$ lies in the inertial wave frequency range. We also test the dispersion properties of the waves by computing the spectral energy as a function of frequency, ϖ, and the dispersion angle, θ. Our results suggest that the columnar flow in the rotation-dominated core, which is an important ingredient for the maintenance of a dipolar magnetic field, is maintained despite the chaotic evolution of the buoyancy field on a fast-time scale by internally-driven inertial waves.

Key words: Inertial waves, Buoyancy-driven flows, Columnar flow

2   *Ranjan et al.*

1   INTRODUCTION

Columnar vortices aligned with the rotation axis and spanning much of the Earth's core are thought to be a major element of the motion in the fluid core (Gubbins & Bloxham 1987; Holme 2015). They are a robust feature of many dynamo simulations with rapid rotation (Christensen & Wicht 2015) and they play an essential role for the generation of a dipolar magnetic field (Busse 1975; Kageyama & Sato 1997; Olson, Christensen & Glatzmaier 1999). These are sometimes interpreted as columnar eigenmodes of non-magnetic convection in a rapidly rotating sphere. The solution of this linear boundary-value problem (Busse 1970) is influenced by the sloping spherical boundary (Greenspan 1968) and assumes a weak time-dependence of the velocity field in the azimuthal direction. However, this assumption is rarely met in strongly forced dynamo simulations with vigorous and highly unsteady thermal convection, and it is hardly justified for the Earth's core. For example, in recent strong-field geodynamo simulations (Yadav et al. 2016; Schaeffer et al. 2017) with significant thermal forcing, i.e. $Ra >> Ra_{crit}$, the flow is observed to be dominated by thin columnar vortices, yet the motion is distinctly unsteady. Here Ra is the Rayleigh number which measures the strength of convection and Ra_{crit} is the value of Ra at which non-magnetic convection is first realised. So, how is the coherence of the columnar structures in the core maintained when the flow, or the distribution of buoyancy forces, changes rapidly with time? The buoyancy forces that drive flow outside the inner-core tangent cylinder, an imaginary cylinder parallel to the rotation axis and touching the inner-core at the equator, tend to be concentrated near the equatorial plane (Olson, Christensen & Glatzmaier 1999; Sakuraba & Roberts 2009). We suggest here that the mechanism by which the columns can follow nearly instantaneously the redistribution of the buoyancy forces is through the spontaneous emission of low-frequency inertial wave packets that travel preferentially away from the equatorial plane in the direction parallel to the rotation axis.

Inertial waves arise as a consequence of the restoring action of the Coriolis force in a rapidly rotating system. They have a frequency given by $\varpi = \pm 2\Omega \cos\theta$, where θ is the orientation of the wave vector $\boldsymbol{\kappa}$ with respect to the rotation vector $\boldsymbol{\Omega}$ (Greenspan 1968). An important property of these waves is that the group velocity,

$$\boldsymbol{C_g} = \pm \frac{2\boldsymbol{\kappa} \times (\boldsymbol{\Omega} \times \boldsymbol{\kappa})}{\kappa^3} = \pm \frac{2\Omega}{\kappa} \left(\hat{\boldsymbol{e}}_\Omega - \cos\theta \hat{\boldsymbol{e}}_\kappa \right), \tag{1}$$

which represents the direction in which wave packets and energy travel, is at right angle to $\boldsymbol{\kappa}$ (Fig. 1), where $\hat{\boldsymbol{e}}_\Omega$, $\hat{\boldsymbol{e}}_\kappa$ are unit vectors along $\boldsymbol{\Omega}$ and $\boldsymbol{\kappa}$ respectively. Moreover, since $\hat{\boldsymbol{e}}_\Omega \cdot \hat{\boldsymbol{e}}_\kappa = \cos\theta$, the component of group velocity parallel to the rotation axis is $C_{g\Omega} = \pm 2\Omega \sin^2\theta/\kappa$ and the magnitude of group velocity is $C_g = 2\Omega|\sin\theta|/\kappa$. Particularly important are the low-frequency inertial wave packets, with $\varpi \approx 0$, that travel nearly parallel to $\boldsymbol{\Omega}$ with the group speed $C_g \approx 2\Omega/\kappa$. It is useful to
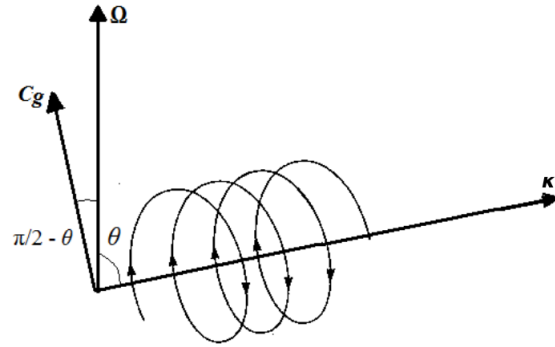
Figure 1. Dispersion properties of an inertial wave. The particle motion is helical.

note that the magnitude of the group velocity is largest for the low-frequency waves (often referred to in the literature as the 'slow waves') and drops to zero for inertial waves with frequency $\varpi \approx 2\Omega$ (or the 'fast waves').

The low-frequency inertial waves are known to create a Taylor column above a slowly moving object in a rotating tank (Taylor 1921). Interestingly, a localized vortex (Tilgner 2000; Davidson et al. 2006) or a buoyant blob (Loper 2001; Davidson 2014) can also radiate low-frequency inertial wave packets leading to the formation of columnar flow structures (Ranjan & Davidson 2014; Davidson & Ranjan 2015). Moreover, those waves which travel parallel to the rotation vector have negative helicity, $\boldsymbol{u} \cdot (\nabla \times \boldsymbol{u}) < 0$, and those that travel anti-parallel have positive helicity (Moffatt 1970). This property of a monochromatic wave extends to inertial wave packets as well (Ranjan 2017). Although governed by the same set of equations, the formation of a Taylor column is different to the generation of a columnar structure by an eddy or blob (Fig. 2a,b) in the sense that the former is boundary-driven with a prescribed time scale, where as the latter is internally-driven with no prescribed time scale (Davidson et al. 2006; Davidson 2013, 2014).

To understand columnar structure formation from a buoyant blob, let us consider the relevant governing equations. In a rotating reference frame, a flow with low viscosity and strong rotation (i.e. the advection of momentum negligible compared to the Coriolis force) is governed by

$$\frac{\partial \boldsymbol{u}}{\partial t} = -\frac{1}{\rho}\nabla \tilde{p} - 2\boldsymbol{\Omega} \times \boldsymbol{u} - \alpha T \boldsymbol{g}, \tag{2}$$

under the Boussinesq approximation, where T is the temperature perturbation, α the coefficient of expansion and $\tilde{p}$ the dynamic pressure which includes the centrifugal force. The corresponding evolution equation for vorticity, $\boldsymbol{\omega} = \nabla \times \boldsymbol{u}$, is

$$\frac{\partial \boldsymbol{\omega}}{\partial t} = 2(\boldsymbol{\Omega} \cdot \nabla)\boldsymbol{u} - \alpha \nabla T \times \boldsymbol{g}. \tag{3}$$

By applying the curl ($\nabla \times$) once again, then taking $\partial/\partial t$, and using $\nabla \cdot \boldsymbol{u} = 0$ we get,
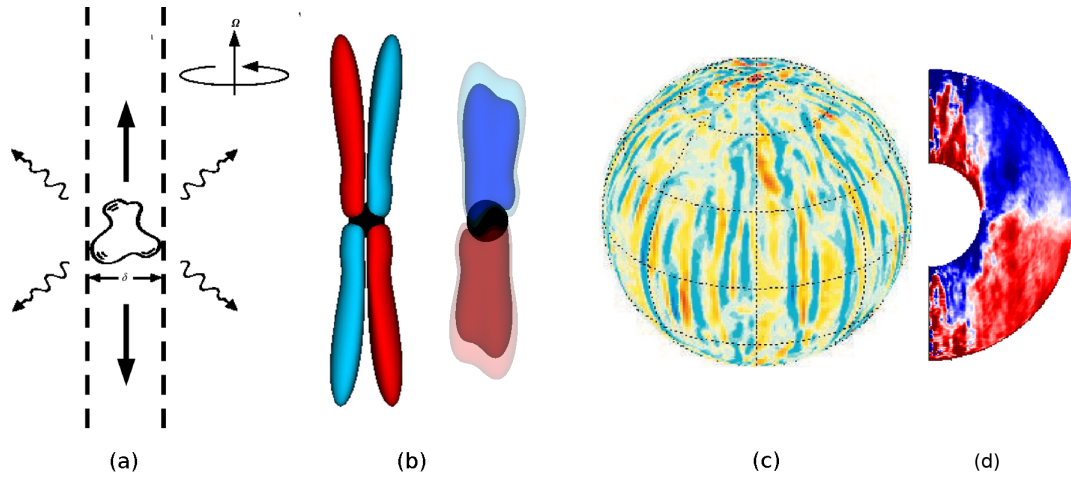
4   *Ranjan et al.*

Figure 2. (a) Preferential radiation of low-frequency inertial wave packets from an eddy along $\boldsymbol{\Omega}$ leads to the formation of columnar structures (Davidson et al. 2006). (b) Alternate cyclone/anti-cyclone pair above and below the buoyant blob (a localized buoyant anomaly that can be of arbitrary shape) shown in black (Davidson & Ranjan 2015); the image on left shows u_z, while the image on right shows helicity. A cyclone has the same sense of rotation as the background, anti-cyclone has the opposite. (c) Radial velocity at the outer boundary and (d) azimuthally-averaged helicity in the present simulation. Red is positive, blue negative.

$$\frac{\partial^2}{\partial t^2}(\nabla^2 \boldsymbol{u}) + 4(\boldsymbol{\Omega} \cdot \nabla)^2 \boldsymbol{u} = 2\alpha(\boldsymbol{\Omega} \cdot \nabla)(\nabla T \times \boldsymbol{g}) + \alpha \nabla \times \left(\nabla \frac{\partial T}{\partial t} \times \boldsymbol{g}\right). \tag{4}$$

If T evolves slowly on the fast time-scale of inertial waves, then we have the wave equation

$$\frac{\partial^2}{\partial t^2}(\nabla^2 \boldsymbol{u}) + 4(\boldsymbol{\Omega} \cdot \nabla)^2 \boldsymbol{u} = 2\alpha(\boldsymbol{\Omega} \cdot \nabla)(\nabla T \times \boldsymbol{g}). \tag{5}$$

Moreover, the evolution of the z-component of vorticity, which is particularly relevant for this study, is

$$\frac{\partial \omega_z}{\partial t} = 2\Omega \frac{\partial u_z}{\partial z} - \frac{\alpha g_o}{r_o} \frac{\partial T}{\partial \phi}, \tag{6}$$

in cylindrical (s, ϕ, z) coordinates, where we have assumed a gravity that increases linearly with radius, $\boldsymbol{g} = -g_o \boldsymbol{r}/r_o$, g_o is the gravity at the outer boundary and $\boldsymbol{\Omega} = \Omega \hat{\boldsymbol{e}}_z$. Here it is important to note that the terms on the right-hand-side of (5) and (6), containing $\partial T/\partial \phi$, act as a localized source of inertial wave packets which propagate away from any buoyant blob to create columnar flow structures (Fig. 2b).

The flow generated by a single buoyant blob resembles the columnar vortices aligned with the rotation axis observed in dynamo simulations (Fig. 2c), taking the form of cyclone/anti-cyclone pairs above and below the blob, with negative helicity above and positive below. Naturally, this leads one to ask if the mechanism of column formation by low-frequency inertial waves could be important in the core (Davidson 2014), where a preferential concentration of buoyancy near the equatorial plane is

expected (Olson, Christensen & Glatzmaier 1999; Sakuraba & Roberts 2009). In this study, we investigate this question by conducting a statistical analysis of the output obtained from a strongly-forced geodynamo simulation. The question is an important one, as efficient planetary dynamos require the azimuthally-averaged helicity to be of one sign in the north and another in the south (Fig. 2c). The origin of this spatial segregation in helicity is still unknown, but it is argued in Davidson & Ranjan (2015) that inertial waves launched in and around the equator represent a good candidate for maintaining such a helicity distribution.

2   GEOYNAMO SIMULATION AT MODERATELY HIGH RAYLEIGH NUMBER

The geodynamo simulation is carried out using the open source MagIC code (Wicht 2002), available at https://github.com/magic-sph/magic, which solves the governing equations for an electrically conducting Boussinesq fluid in a rotating spherical shell with an aspect ratio representative of the outer core, $r_i/r_o = 0.35$. The dimensionless equations are

$$\frac{\partial \boldsymbol{u}}{\partial \mathrm{t}} + (\boldsymbol{u} \cdot \nabla)\boldsymbol{u} = -\nabla \tilde{p} - \frac{2\hat{\boldsymbol{e}}_z \times \boldsymbol{u}}{E} + \frac{Ra}{Pr}\frac{T\boldsymbol{r}}{r_o} + \frac{(\nabla \times \boldsymbol{B}) \times \boldsymbol{B}}{EPm} + \nabla^2 \boldsymbol{u}, \tag{7}$$

$$\frac{\partial \boldsymbol{B}}{\partial \mathrm{t}} = \nabla \times (\boldsymbol{u} \times \boldsymbol{B}) + \frac{1}{Pm}\nabla^2 \boldsymbol{B}, \tag{8}$$

$$\frac{\partial T}{\partial \mathrm{t}} + (\boldsymbol{u} \cdot \nabla)T = \frac{1}{Pr}\nabla^2 T, \tag{9}$$

$$\nabla \cdot \boldsymbol{u} = \nabla \cdot \boldsymbol{B} = 0, \tag{10}$$

where $Ra = \alpha g_o d^3 \Delta T/\nu\kappa$, $E = \nu/\Omega d^2$ (Ekman number), $Pr = \nu/\kappa$ (Prandtl number), $Pm = \nu/\lambda$ (magnetic Prandtl number) are the control parameters. In the dynamo model, time is non-dimensionalized by d^2/ν, length by the shell thickness $d = r_o - r_i$, temperature perturbation by the difference $\Delta T = (T_o - T_i)$, and magnetic field by $\sqrt{\mu\lambda\rho\Omega}$. Here α is the thermal expansion coefficient, ν is the kinematic viscosity, ρ is the background reference density, μ is the magnetic permeability, and κ, λ are the thermal and magnetic diffusivities. The velocity and magnetic field vectors are decomposed into toroidal and poloidal potentials which guarantees their zero-divergence. The governing equations are written in terms of these potentials, converted into spectral space using Chebyshev polynomials in the radial (r) direction and spherical harmonic decomposition in the azimuthal (ϕ) and latitudinal (θ) directions, and then numerically integrated. The time-advancement is done using an explicit second-order Adams–Bashforth scheme for the nonlinear terms and the implicit Crank–Nicolson algorithm for the linear terms (more details are in Christensen & Wicht (2015)).

The control parameters in our simulation are $Ra = 1.2 \times 10^8$ ($Ra/Ra_{crit} = 42.4$), $E = 3 \times 10^{-5}$, $Pr = 1$, $Pm = 2.5$. This parameter set was chosen so that the flow is sufficiently unsteady for waves to exist. Also, its magnetic field morphology on the outer boundary is rather Earth-like according

6   *Ranjan et al.*

to the criteria of Christensen et al. (2010). The thermal boundary conditions are in terms of fixed temperatures at the inner and outer boundaries. Both boundaries have no-slip boundary condition and are assumed to be electrically insulated. The simulation is first run for 0.1 magnetic diffusion times (~ 100 advection time scales) in which the dynamo reaches a statistical equilibrium state. The Courant condition is maintained with a very small time-step so as to resolve inertial waves. At the end of the run, the values of the diagnostic parameters are $Rm = 902$, $\Lambda = 27$, $Ro = 0.01$ where Rm, Λ, Ro, are the magnetic Reynolds number, the Elsasser number and the Rossby number, defined as

$$Rm = \frac{ud}{\lambda}, \quad \Lambda = \frac{B^2}{\mu\lambda\rho\Omega}, \quad Ro = \frac{u}{\Omega d}.$$

With the same time-step, the simulation is re-started (at $\Omega t = 0$) and we record all variables with high time resolution for a short interval of 0.0016 diffusion times, which corresponds to $\Omega t = 133.4$ or $\approx$ 21 Earth days using $\Omega = 7.29 \times 10^{-5} rad/s$. (Note that, hereafter, we use Ωt as the non-dimensional unit of time).

The radial magnetic field is dipolar with opposite polarity flux spots at low latitudes (Supplementary Information Fig. S1). For $\Omega t = 0$, Figs. 3a-d show the equatorial cross-sections of u_z, ω_z, T and $\partial T/\partial\phi$, where T is the temperature perturbation or anomaly above the conducting reference. The small-scale flow structure of ω_z (Fig. 3b) closely resembles that of $\partial T/\partial\phi$ (Fig. 3d), which is to be expected from equation (6).

We move to cylindrical co-ordinates (s, ϕ, z) in order to study the dynamics parallel to $\mathbf{\Omega}$ (Appendix A). The $\phi - z$ slices of u_z, ω_z, T and $\partial T/\partial\phi$ at a cylindrical radius of $s = 0.62d$ are shown in Figs. 3e-h. (For reference, the inner boundary is at $s_i = 0.53d$ and the outer boundary at $s_o = 1.53d$. We have deliberately kept these quantities dimensional in order to avoid confusion with the group velocity calculations later on.) The flow is evidently columnar. Moreover, the thermal source of inertial waves outside the tangent cylinder is concentrated near the equator, as is evident from Fig. 3i which shows the r.m.s. of $\partial T/\partial\phi$, i.e. $(\langle(\partial T/\partial\phi)^2\rangle_\phi)^{1/2}$, where $\langle\ \rangle_\phi$ denotes azimuthal-average.

As a measure of the columnarity, the quantity

$$C(s, \phi) = \left[\frac{(\langle\omega_z\rangle_z)^2}{\langle\omega_z^2\rangle_z}\right]^{1/2} \tag{11}$$

is shown in Fig. 4a, where $\langle\cdot\rangle_z$ denotes vertical average. (A similar definition of columnarity was considered by Soderlund et al. (2012) in which only the non-axisymmetric part of the velocity field was used to calculate vorticity.) The average columnarity outside the tangent cylinder is $C \approx 0.38$, but some regions are clearly more columnar than the others, the maximum value of C being 0.99. (The value of columnarity as defined in Soderlund et al. (2012) is also 0.38 in our simulation.) The ϕ-average of C increases with s as we move further from the tangent cylinder, after which it becomes roughly constant in the bulk, as evident from Fig. 4b. Interestingly, the spatial distribution of

Table 1. Comparison of observed slopes for the light green lines in Fig. 5a-d with the estimated slope calculated from the group speed of low-frequency inertial waves, $C_g \approx 2\Omega/(\pi/\delta_h) = z/t$. δ_h is measured directly from the plot of ω_z.

$(s/d, \phi)$	Slope in the $z/d - \Omega t$ plot of $\dot{u}_z$	δ_h/d	Estimated slope, $2\delta_h/\pi d$
$(0.62, 0.376)$	0.03	0.05 ± 0.005	0.032 ± 0.003
$(0.62, 5.89)$	0.06	0.086 ± 0.006	0.055 ± 0.004
$(0.99, 2.50)$	0.047	0.07 ± 0.005	0.044 ± 0.003
$(0.99, 6.14)$	0.04	0.06 ± 0.005	0.038 ± 0.003

$C(s, \phi)$ closely matches that of $\partial T/\partial \phi$, the source of inertial waves, shown in (Fig. 3d), suggesting that the low-frequency inertial waves triggered near the equator could be important for maintaining the columnarity. Indeed, a spatial cross-correlation of $|\partial T/\partial \phi|$ at $z = 0$ with C, calculated as

$$R_C(r_s, r_\phi) = \frac{\int_0^{2\pi} \int_{s_i}^{s_o} |T_\phi(s, \phi)| C(s + r_s, \phi + r_\phi) ds d\phi}{[\int_0^{2\pi} \int_{s_i}^{s_o} |T_\phi(s, \phi)|^2 ds d\phi \int_0^{2\pi} \int_{s_i}^{s_o} C(s, \phi)^2 ds d\phi]^{1/2}}, \tag{12}$$

where $T_\phi = \partial T/\partial \phi$, and (r_s, r_ϕ) are the lags along (s, ϕ), respectively. Figure 4c shows a peak value of $R_C \approx 0.57$ occurring at $(r_s, r_\phi) = (0, 0)$. The cross-correlation is stronger for negative r_s due to the fact that regions near the inner boundary are not as columnar as those in the bulk. As a result, a negative lag or shift along s in the distribution of C leads to a stronger correlation with $|\partial T/\partial \phi|$.

2.1 Temporal evolution

The temporal evolution of the buoyancy field shows that it is closely linked to changes in the columnar features of the velocity field (see movies ms1-5 in Supplementary Information), necessitating inspection at closer time-intervals. We therefore consider time-series of the velocity and buoyancy fields for the duration $\Omega t = [0, 133.4]$ with a high temporal resolution, $\Omega \Delta t = 0.133$. (The results are the same at smaller values of $\Omega \Delta t$). Since the presence of a wave-front is closely related to $\partial \boldsymbol{u}/\partial t$ in the momentum equation (2), we focus on

$$\dot{u}_z = -\frac{\Delta u_z}{\Omega \Delta t} \tag{13}$$

as a diagnostic, where Δu_z denotes a change in u_z over the time Δt. Note that $\dot{u}_z$ is indicative of the rate at which information (or energy) is propagated vertically by wave fronts in low-frequency inertial waves, $\varpi \ll 2\Omega$, as well as the internal motion in higher frequency waves, $\varpi \sim \Omega$. In the analysis presented hereafter, since $\Omega \Delta t$ is fixed, $\dot{u}_z$ is the same as $-\Delta u_z$ without the division by 0.133. Moreover, we choose the northern hemisphere for illustration.
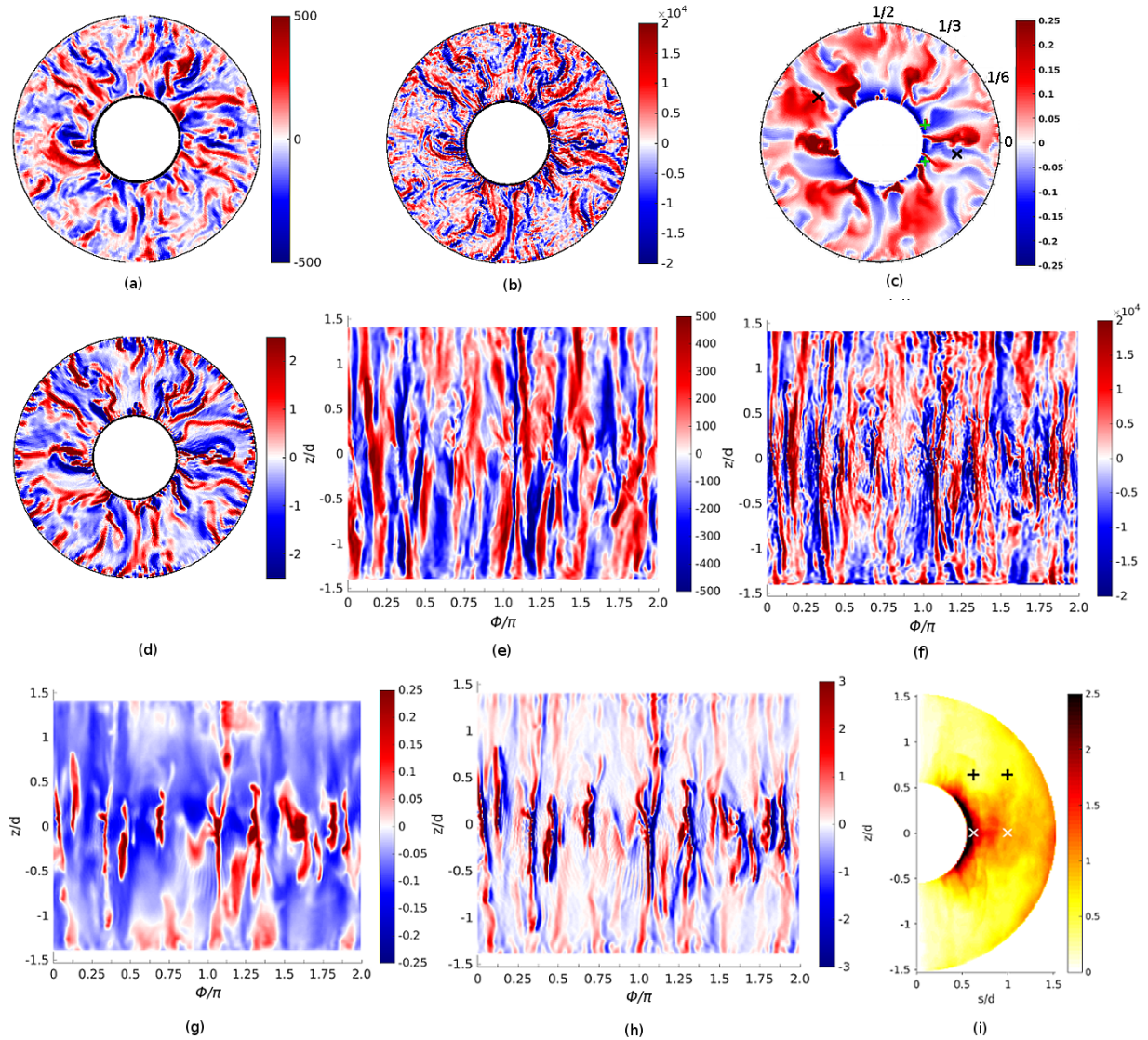
8   *Ranjan et al.*

Figure 3. (a-d) Equatorial-slices of u_z, ω_z, T and $\partial T/\partial\phi$ respectively, and (e-h) their $\phi - z$ slices at $s = 0.62d$. (i) $(\langle(\partial T/\partial\phi)^2\rangle_\phi)^{1/2}$. All images are at $\Omega t = 0$. In (c), the numbers near the outer boundary represent ϕ/π. In (c) and (i), the symbols $+$ and $\times$ denote the points chosen for time-series analysis in §2.1.1, 2.1.2.

2.1.1   Time-distance plots

Here the word 'distance' means 'vertical distance'. To study the vertical-propagation of inertial waves, we choose four locations on the equatorial plane $(s/d, \phi) =$ (i) $(0.62, 0.376)$, (ii) $(0.62, 5.89)$, (iii) $(0.99, 2.5)$, and (iv) $(0.99, 6.14)$, which are marked in Fig. 3c. (Note for reference that $0.62d = 0.40r_o$ and $0.99d = 0.64r_o$). These locations are based on the criteria that there are no significant sources of buoyancy near the outer boundary vertically-above the location, i.e. at the same (s, ϕ), at any time. This is because such sources might initiate downward-propagating waves near the mantle and hence influence the signature of waves triggered by buoyant regions near the equator. Also, the chosen loca-
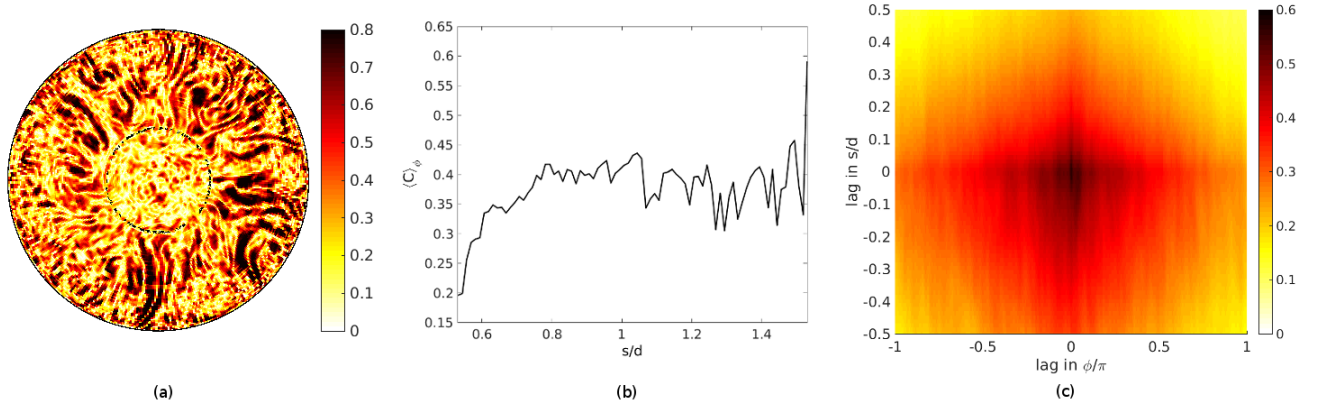
Figure 4. At $\Omega t = 0$, (a) columnarity $C(s, \phi)$, defined in (11), (b) $\langle C \rangle_\phi$ and (c) the cross-correlation of the $|\partial T/\partial \phi|$ (Fig. 3d) with C.

tions are outside any boundary layers. The time-distance plots for $\dot{u}_z$ at these four locations, computed on a line that extends from the equatorial plane to the outer boundary, are shown in Figs. 5a-d. In these plots, it is interesting to see positive slopes that are linked to the rate at which energy is propagating vertically upwards by low-frequency inertial wave-fronts. Negative slopes are less common, but present, and may represent reflections from the outer boundary. The corresponding time-distance plots of u_z and $\partial T/\partial \phi$ are shown in Supplementary Information Figs. S2, S3. While most of the slopes represent inertial wave propagation aligned or nearly-aligned to the rotation axis, certain features in Fig. 5 appear to be nearly vertical. These are most likely vertically-extended convective features moving past the chosen longitude. Since the waves and their thermal source co-exist in most locations, particularly near the equator, it is difficult to apply any external filter to the data to eliminate such features.

For quantitative analysis, we first compute the slopes at four representative fronts indicated by light green lines in Fig. 5a-d and compare with those expected from the group speed of low-frequency inertial waves given by $C_g \approx 2\Omega\delta_h/\pi$ (using $\kappa \approx \pi/\delta_h$) (Davidson 2004, p. 373). Here δ_h is the local azimuthal length scale at the location where these waves arise, scaled by the shell thickness d and measured directly from the z-vorticity field at the appropriate (s, ϕ, z, t) location. For example, from the plots of ω_z shown in Figs. 3b and 3f, $\delta_h \approx 0.05d$ for $(s/d, \phi) = (0.62, 0.376)$. ($\delta_h$ is approximately the same at a higher $z/d \approx 0.8$ as the structure is columnar.) Therefore, the estimated slope is $(z/d)/(\Omega t) \approx 0.032$, very close to the observed slope of the corresponding green line, 0.03. Table 1 shows that there is an excellent agreement between the estimated and observed slopes for all four points in Fig. 5a-d.

At this point, it is natural to ask if there are inertial waves of higher frequency present in the simulation. To answer this, we compute the fast Fourier transform (FFT) of $\dot{u}_z(z, t)$ corresponding to the same four locations used in Fig. 5. In Fig. 6 we show the corresponding FFTs, $\mathcal{F}(\dot{u}_z)$, as a
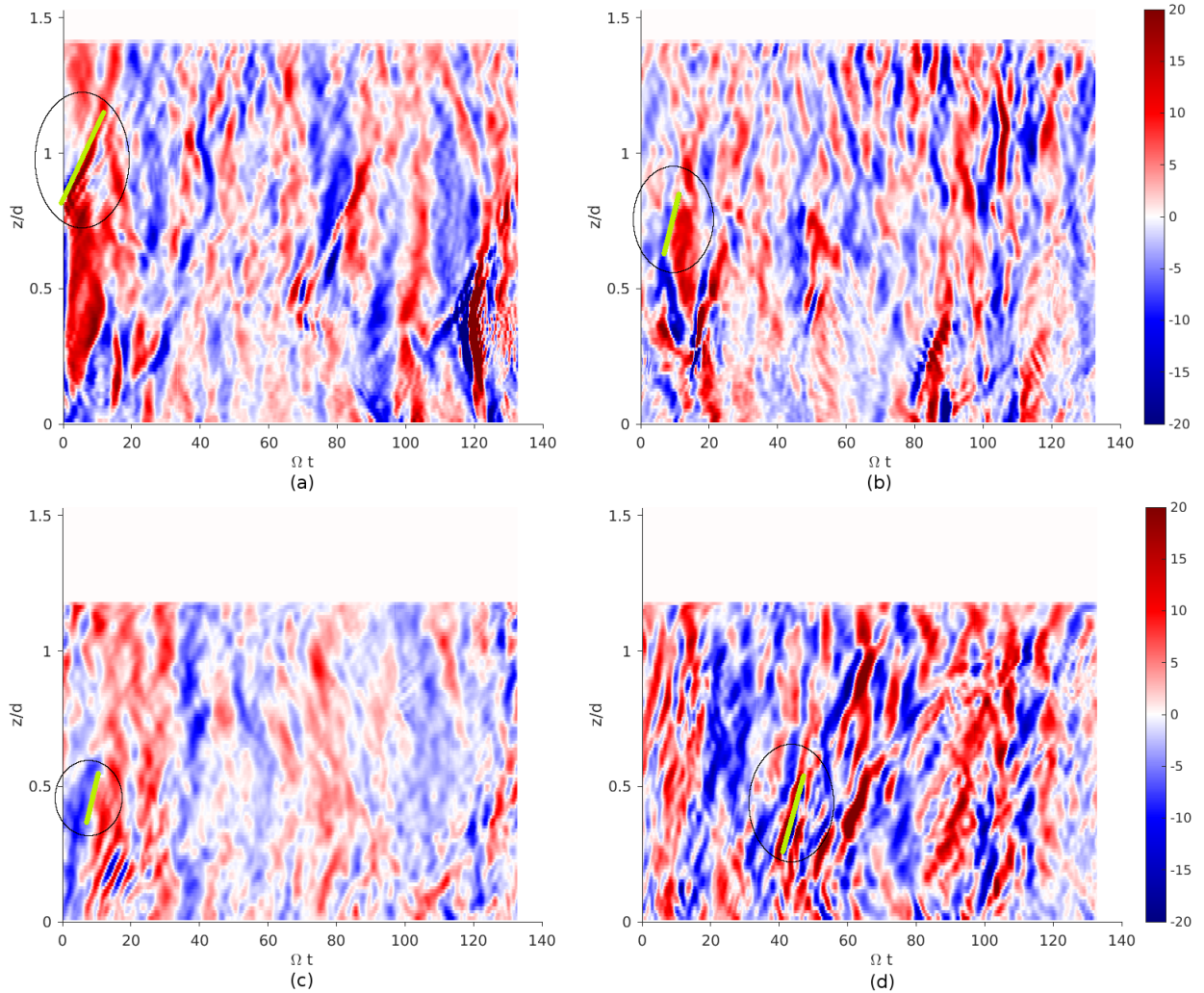
10   *Ranjan et al.*

Figure 5. Time-distance plots of $\dot{u}_z$ for (a)$(s/d, \phi) = (0.62, 0.376)$, (b) $(0.62, 5.89)$, (c) $(0.99, 2.50)$ and (d) $(0.99, 6.14)$. The light green lines (located by ellipses) are used to calculated slopes in Table 1.

function of (k_z, ϖ_T), from which it is evident that the spectrum is broadband, although the peaks are at low frequency. (Note that (k_z, ϖ_T) refer to the wave number and frequency in the Fourier analysis while (κ, ϖ) denote the wave number and frequency of an inertial wave.) Moreover, i these plots, the second and fourth quadrants denote the waves propagating away from the equator and the first and third quadrants denote the waves propagating towards the equator.

Of course, there is some subjectivity in the choice of the four locations used in Figs. 5, 6 and Table 1. For an objective statistical analysis, we compute the FFTs of all $\dot{u}_z$ plots (such as those in Fig. 5a-d) along ϕ at a fixed s, and average the FFTs to obtain $\langle|\mathcal{F}(\dot{u}_z)|\rangle_\phi$. This yields an asymmetric butterfly-shaped spectrum for both the s locations, as indicated in Fig. 7a,b. Remarkably, the frequency range in Figs. 6 and 7a,b is exactly what we would expect for inertial waves, $0 \leq |\varpi|/\Omega \leq 2$,
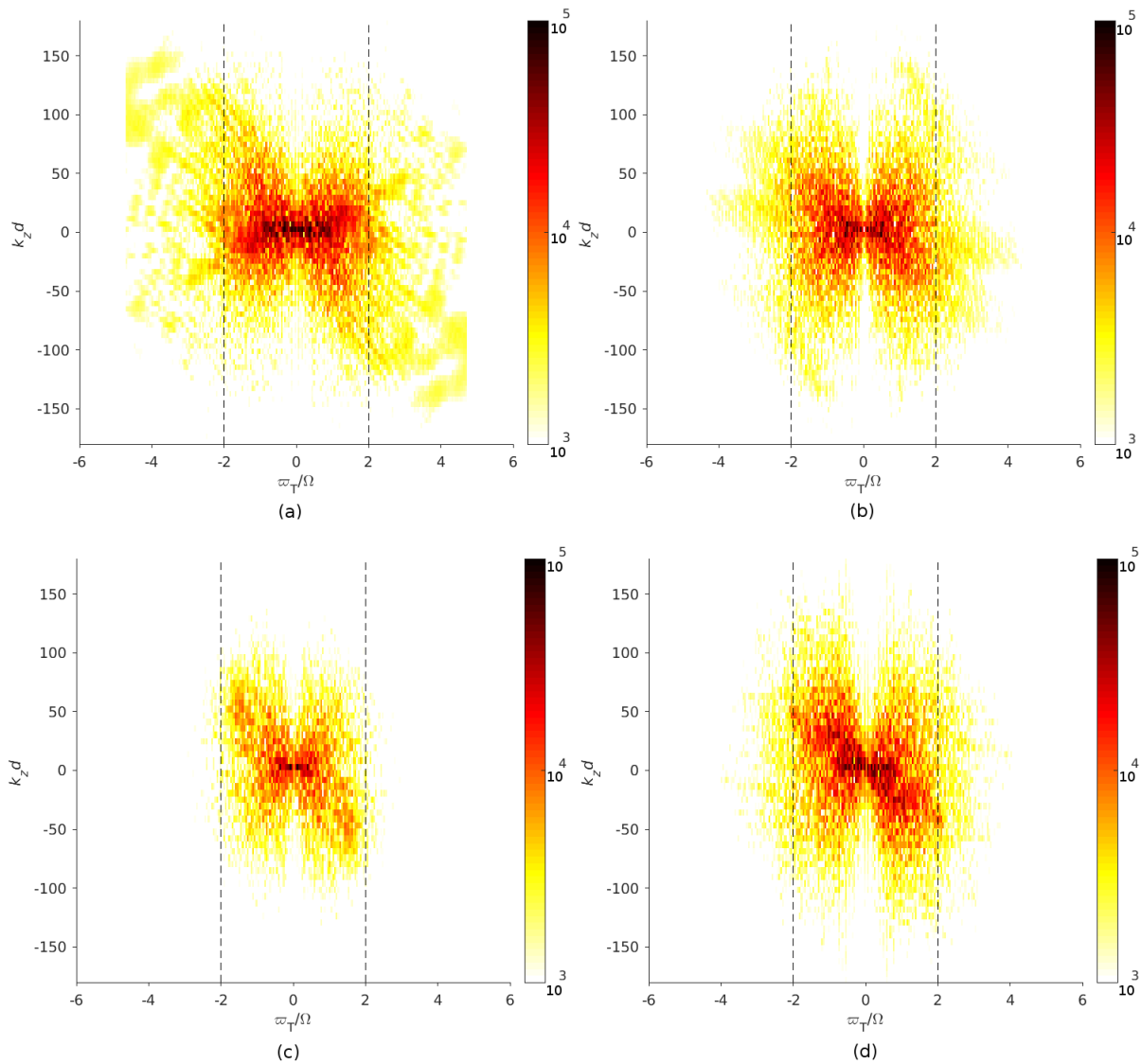
Figure 6. $|\mathcal{F}(\dot{u}_z)|$ for the plots corresponding to the four locations (a)$(s/d, \phi) = (0.62, 0.376)$, (b) $(0.62, 5.89)$, (c) $(0.99, 2.50)$ and (d) $(0.99, 6.14)$, shown in Fig. 5. The dotted lines show the inertial wave frequency range, $0 \leq |\varpi|/\Omega \leq 2$.

and captures nearly all the energy in the spectral plot. The peaks in the spectra are observed to be concentrated at low frequencies, also evident by zooming in on the central regions shown in Fig. 7c,d. However, it is difficult to conclude that all energy near low frequencies is from inertial waves as some contribution may also come from advection. The asymmetry between the 'butterfly-wings' shows that waves propagating away from the equator are statistically more prevalent than those travelling towards the equator (triggered by buoyant anomalies far from the equator or arising due to reflections at the boundary).
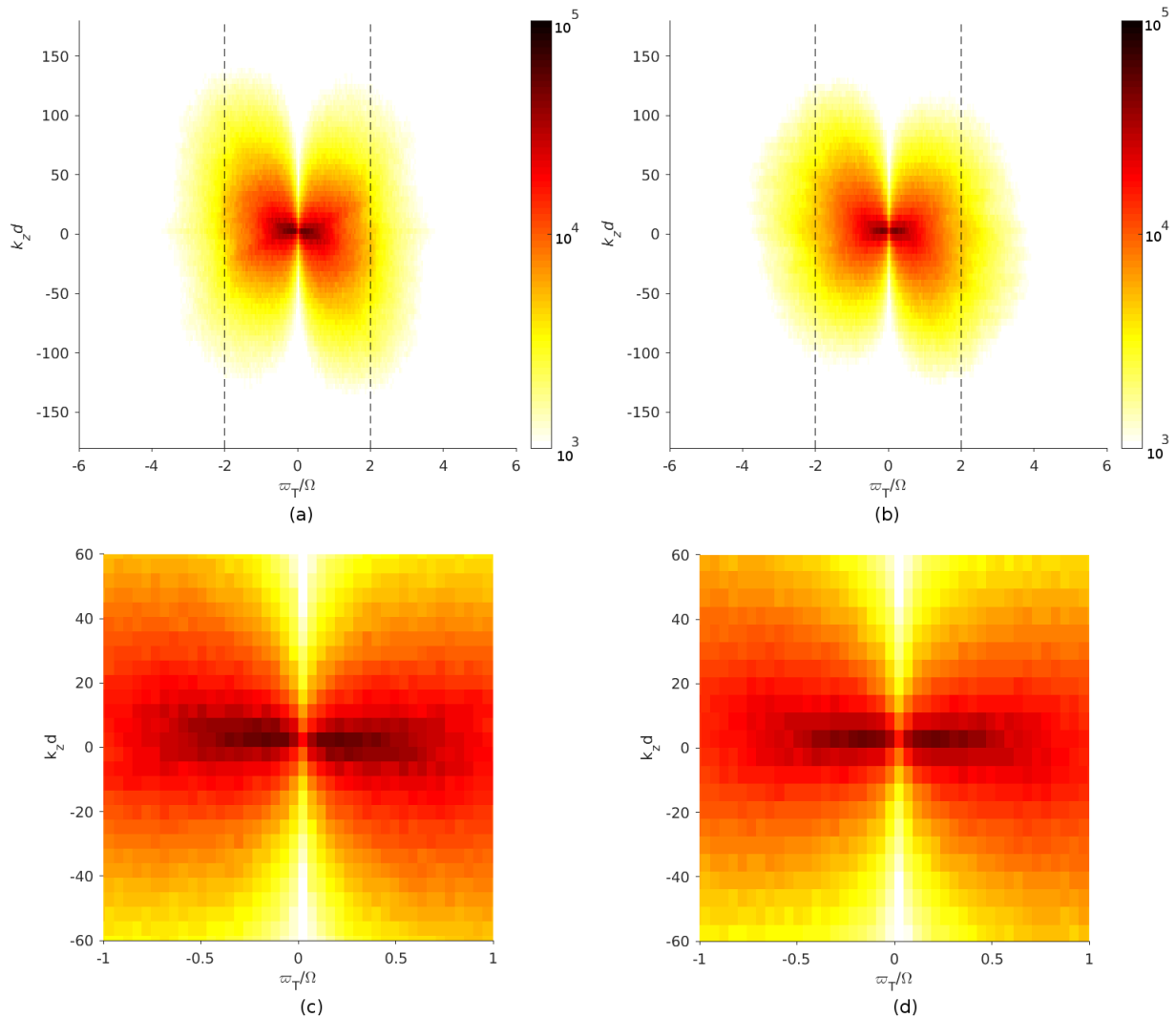
12   *Ranjan et al.*

Figure 7. The ϕ-averaged spectrum of $\dot{u}_z$ i.e. $\langle|\mathcal{F}(\dot{u}_z)|\rangle_\phi$ for (a) $s = 0.62d$, (b) $s = 0.99d$. The dotted lines show the inertial wave frequency range, $0 \leq |\varpi|/\Omega \leq 2$. (c-d) Same as (a-b) but zoomed in the central region.

2.1.2 *Longitude-time plots*

Let us now move to the longitude-time plots of $\partial T/\partial \phi$ and $\dot{u}_z$. For this purpose, we choose a point in (s, z) and obtain a plot of the appropriate variable with ϕ on the horizontal axis and time on the vertical. Such a plot is essentially a time-series on a circle with fixed cylindrical radius. Figures 8a,b show the ϕ-t plots of $\partial T/\partial \phi$ for two radial locations at the equator (marked in Fig. 3i), $(z/d, s/d) = (0, 0.62)$ and $(0, 0.99)$, respectively. Black lines with positive (negative) slopes represent eastward (westward) movements in the buoyancy field at the equator. The longitude-time plots of $\dot{u}_z$ much above the equator (at $z/d = 0.64$) for $s/d = 0.62$ and $s/d = 0.99$ are shown in Fig. 8e,f. Careful visual inspection of

the slopes in Figs. 8a-d suggests that the eastward/westward ϕ movements in the longitude-time plots of $\partial T/\partial \phi$ correspond to similar movements in $\dot{u}_z$, but a statistical cross-correlation is required.

The ϕ-t cross-correlation between $\partial T/\partial \phi$ and $\dot{u}_z$ is calculated using

$$R_{\phi-t}(r_\phi, r_t) = \frac{C_t \int_0^{2\pi} \int_0^{t_m - r_t} |T_\phi'(\phi, t)||\dot{u}_z(\phi + r_\phi, t + r_t)|dt d\phi}{[\int_0^{2\pi} \int_0^{t_m} |T_\phi'(\phi,t)|^2 dt d\phi \int_0^{2\pi} \int_0^{t_m} |\dot{u}_z(\phi,t)|^2 dt d\phi]^{1/2}}, \tag{14}$$

where $T_\phi = \partial T/\partial \phi$, $C_t = t_m/(t_m - r_t)$, (r_ϕ, r_t) are the lags in correlation along (ϕ, t) and $\Omega t_m = 133.4$ is the final time. $(\partial T/\partial \phi)'$ is obtained from $\partial T/\partial \phi$ by subtracting its time-average, i.e. $(\partial T/\partial \phi)' = \partial T/\partial \phi - \langle \partial T/\partial \phi \rangle_t$. Note that in (14) the cross-correlation is multiplied by the pre-factor C_t in order to remove the bias near zero time-lags, which, for instance, is a standard practice in time-distance helioseismology (Gizon & Birch 2005). Also, we have used the absolute values of $(\partial T/\partial \phi)'$ and $\dot{u}_z$ as we are interested in their slopes rather than their signs. The cross-correlation between $(\partial T/\partial \phi)'$ at $z = 0$ and $\dot{u}_z$ at $z/d = 0.64$ is shown in Figs. 8e for $s/d = 0.62$ and 8f for $s/d = 0.99$, respectively. Remarkably, the correlation peak lies at zero lag in ϕ for both the s-locations, confirming that a movement near the equator in ϕ is well-correlated with a movement above at the same horizontal location. With respect to the time-lag, the cross-correlation is similar over a broad range of times, perhaps due to the columnar nature of the flow. However, as a signature of information propagation by inertial waves, we expect to see a peak at a finite (non-zero) time-lag, corresponding to the time of flight calculated from the group speed.

To explore this further, we cross-correlate several pairs of $|(\partial T/\partial \phi)'|$ in the range $0 \leq z/d \leq 0.28$ and $|\dot{u}_z|$ in $0.64 \leq z/d \leq 0.92$ at a fixed vertical separation, $\Delta z = 0.64d$, for both radial locations. The z-averaged cross-correlation, $\langle R_{\phi-t} \rangle_z$, shown in Figs. 9a,b for the two radial locations, resembles those in Figs. 8e-f. At zero lag in ϕ, the variation of $\langle R_{\phi-t} \rangle_z$, with time-lags on the horizontal axis, is shown in Figs. 9c,d. For $s/d = 0.62$, we observe a peak at a positive time-lag of $\Omega t = 26$ (Fig. 9c) whereas for $s/d = 0.99$, the peak occurs at zero time-lag (Fig. 9d). For low-frequency inertial waves, the group speed can be written as (Greenspan 1968)

$$C_g \approx \frac{2\Omega}{\kappa} = \frac{\Delta z}{t_f}, \tag{15}$$

where t_f is the time of flight and κ the wavenumber. The equation (15) strictly holds for a single κ, but can also be used for a slowly-modulated wave packet with a narrow range of wavenumbers. Using the ϕ-spectrum of the z-vorticity field at $s/d = 0.62$ (Fig. 10), we find a dominant wavenumber of $\kappa_\phi = 19\pi/d$. Using (15) with $\Delta z = 0.64d$, we predict that the time-lag should be $\Omega t_f \approx 19$. The peak in Fig. 9c at a lag of $\Omega t = 26$ is close to our estimate based on C_g. This suggests that information is indeed propagated away from the equator by low-frequency inertial wave packets and that the low-frequency inertial waves, travelling parallel to the rotation axis, reinforce the columns and play a major role in maintaining their coherence. However, for the radial location $s/d = 0.99$,
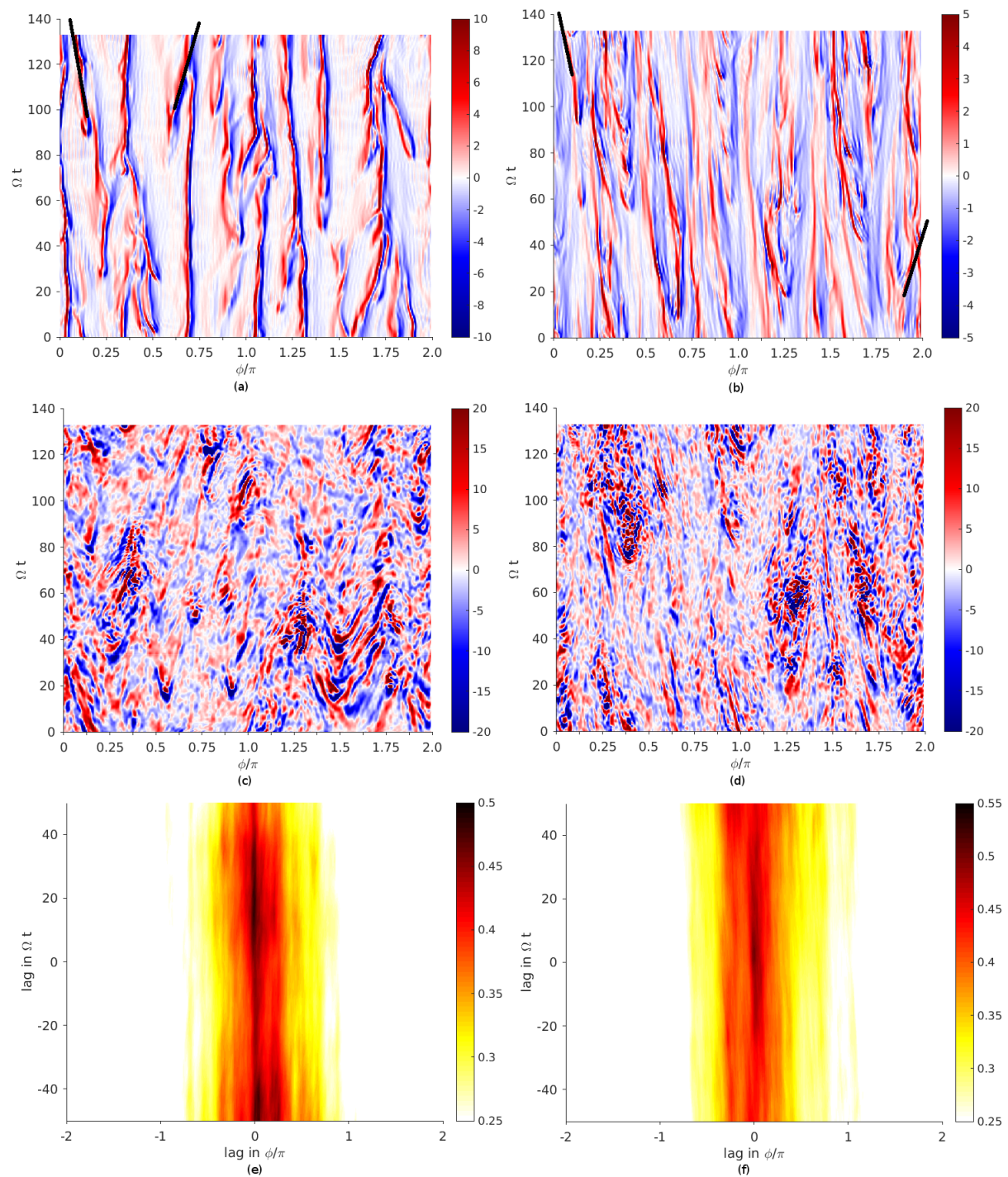
14   *Ranjan et al.*

Figure 8. (a-b) Longitude-time plots of $\partial T/\partial \phi$ at the equator, $z = 0$, for two radial locations $s = 0.62d$ (left) and $s = 0.99d$ (right). The black lines with a negative (positive) slope indicate westward (eastward) movement in T. (c-d) Time series of $\dot{u}_z$ far from the equator at $z = 0.64d$ for the same radial locations. (e-f) Cross-correlation, $R_{\phi-t}$ (14) between $(\partial T/\partial \phi)' = \partial T/\partial \phi - \langle \partial T/\partial \phi \rangle_t$ at $z = 0$ and $\dot{u}_z$ at $z = 0.64d$.

the corresponding group speed estimate for the lag is $\Omega t_f \approx 25$ and while we do observe a secondary peak at this location, the curve in Fig. 9d shows a peak at zero time-lag. This may indicate a pre-existing correlation, or a correlation due to low-frequency inertial waves launched earlier in time from the same (s, ϕ) location on the equatorial plane. Also recall that the flow at large s is observed to be more columnar than that near the tangent cylinder (Fig. 4a,b), perhaps due to reflections at the outer boundary.

Note that we have chosen the z-vorticity field to estimate the wavenumber for two reasons. Firstly, a large part of the Coriolis force in the momentum equation (2) is balanced by the pressure-gradient. Hence, the vorticity equation (3), which represents a non-geostrophic force balance, is more important dynamically (Christensen & Aubert 2006). Secondly, recall that the structure of $\partial T/\partial \phi$, the source of inertial waves, closely resembles that of ω_z (compare Figs. 3b,d). Note also that there is an asymmetry between positive and negative time-lags in Fig. 9c,d for both radial locations, with a larger cross-correlation magnitude for positive time-lags indicating that more waves propagate upwards than downwards.

2.2 Test of dispersion properties using 4D-FFT

So far we have analyzed two-dimensional (z or ϕ, t) time-series which is good for investigating low-frequency inertial waves travelling nearly parallel to the rotation axis. However, recall from the butterfly diagram (Fig. 7) that there could be some off-axis inertial waves present in our numerical dynamo solution. Since, the propagation pattern of these waves is three-dimensional (§1), we now investigate the time-series of $\dot{u}_z(s, \phi, z, t)$ for the duration $\Omega t = [0, 133.4]$, with resolution $\Omega \Delta t = 0.133$. For this purpose, we choose a cylindrical annular domain above the equator, and away from the boundaries, in the region $0.62 \leq s/d \leq 1.21$, $0 \leq \phi/\pi \leq 2$ and $0.33 \leq z/d \leq 0.92$ (the size of this domain is constrained by the spherical geometry). The resulting 4D-computation matrix is of size $(48 \times 384 \times 48 \times 1000)$, with only a modest resolution in space but good resolution in time. We divide this domain into eight boxes of size 48^3 so that the matrix size is the same in all spatial directions, a prerequisite for this analysis. For each box we compute the 4D-FFT of the dataset to get $\mathcal{F}_{4D}(\dot{u}_z(k_s, k_\phi, k_z, \varpi_T))$. The spectral energy is computed as: $E(k_s, k_\phi, k_z, \varpi_T) = |\mathcal{F}_{4D}(\dot{u}_z)|^2$. Finally, by adding all contributions to E for the same angle θ, where $\tan \theta = k_s/k_z$, we obtain $E(\theta, \varpi_T)$. A similar procedure was used to test the dispersion properties of inertial waves by Yarom & Sharon (2014), and recently by Le Reun et al. (2017), in the context of rapidly rotating turbulence.

In Fig. 11a, we show the $E(\theta, \varpi_T)$ for the box corresponding to $0 \leq \phi/\pi \leq 0.25$, and in Fig. 11b $E(\theta, \varpi_T)$ averaged over all eight boxes. Also shown in the same figures are the dispersion curves for inertial waves, $\varpi/\Omega = \pm 2 \cos \theta$, where the plus and minus signs correspond to upward and downward
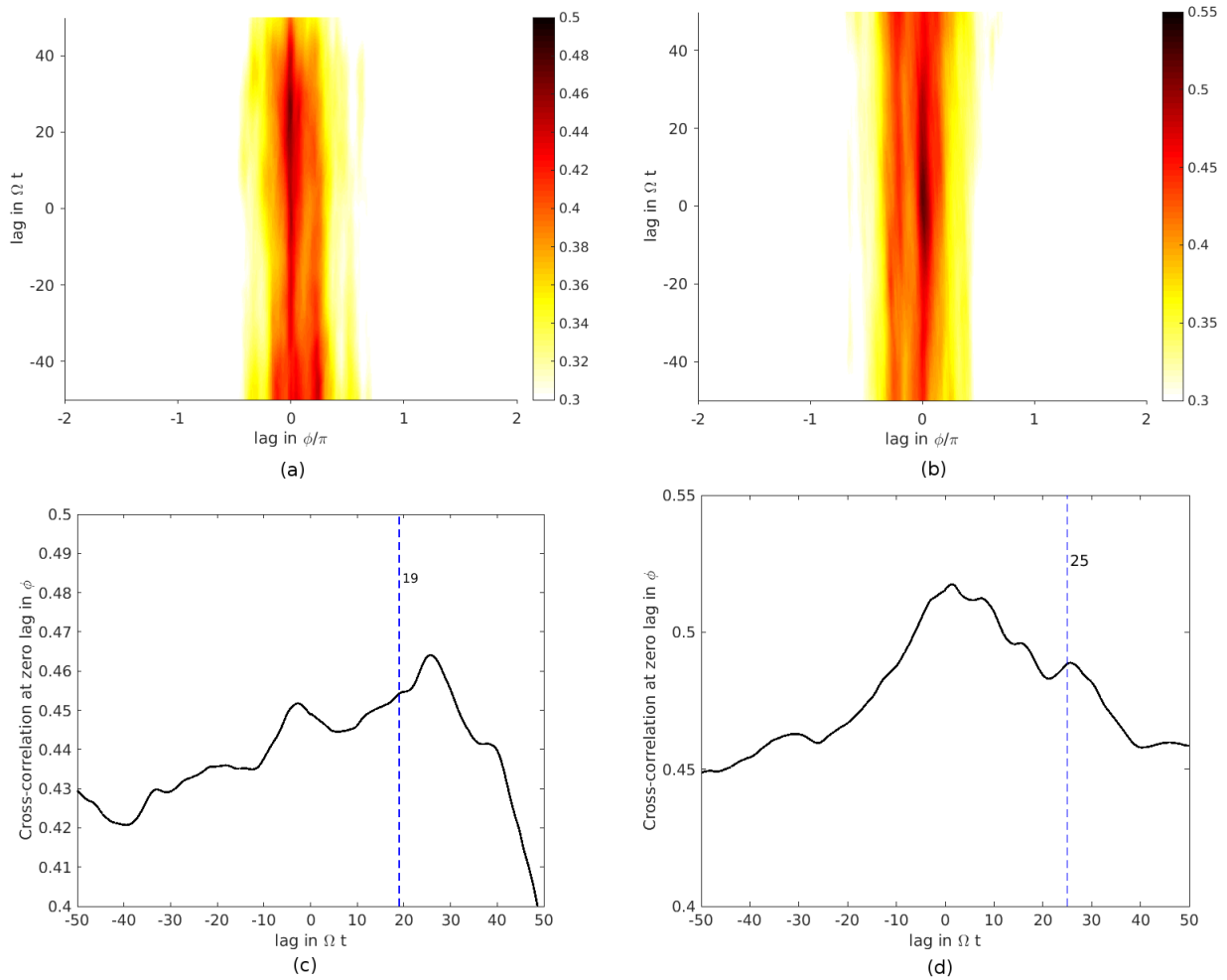
16   *Ranjan et al.*

Figure 9. The z-averaged cross-correlation (14), $\langle R_{\phi-t}\rangle_z$, for the two radial locations (a) $s = 0.62d$ and (b) $s = 0.99d$. For zero lag in ϕ, the $\langle R_{\phi-t}\rangle_z$ as a function of time-lags, for (c) $s = 0.62d$ and (d) $s = 0.99d$.

propagating inertial waves, respectively (§1). The spectral energy sits close to the dispersion curves for the off-axis inertial waves indicating that they are also present in the solution albeit much weaker than the axially-propagating waves. The energy away from the dispersion curves may be due to mean flow or other wave types. Moreover, once again, there is more energy in waves moving away from the equator, than those moving towards the equator. Of course, this reminds us of the asymmetry in the butterfly-diagram (Fig. 7) and in the cross-correlation (Fig. 9) discussed earlier. This asymmetry, along with the strong cross-correlation of the columnarity with the source, $\partial T/\partial \phi$, at the equator (Fig. 4c), strongly suggests that most columns are internally-driven rather than boundary-driven. It also suggests that a significant part of the fast dynamics in the dynamo simulation can be described in terms of low-frequency inertial waves that propagate away from the equatorial plane. Note that the concentration of energy near $\theta = \pi/2$ in Figs. 11a,b could be due to spectral leakage of the energy
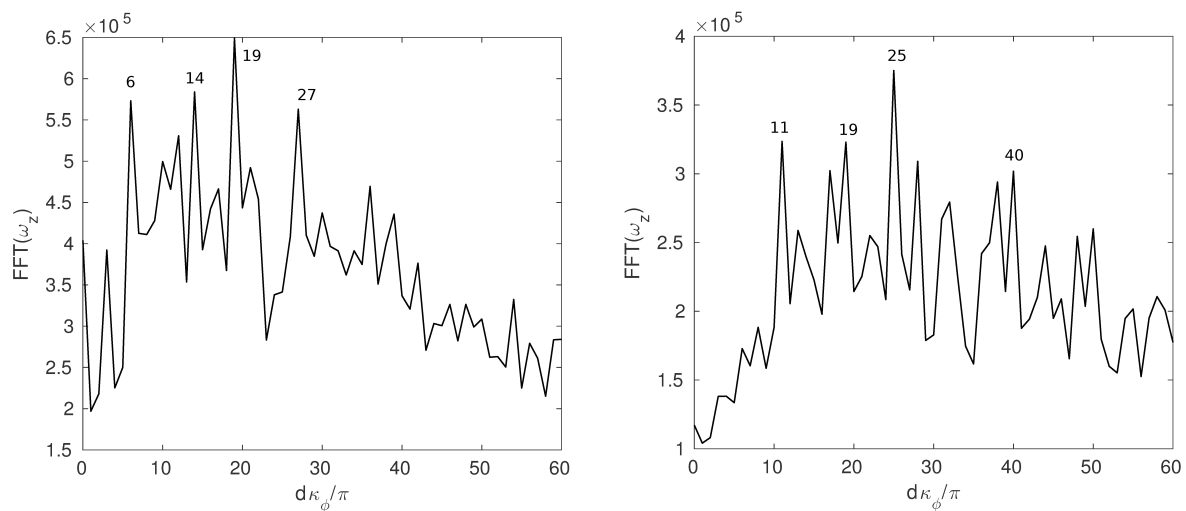
Figure 10. 1-dimensional FFT of z-vorticity, ω_z, averaged over $0 < z/d < 0.28$ near the equator, and over five time co-ordinates in $\Omega t = 0 - 66.7$, for $s = 0.62d$ (left), $s = 0.99d$ (right). The numbers represent the dimensionless azimuthal wave-numbers with large spectral density, and thus the most common length scales at the corresponding radius.

to higher frequencies. Spurious peaks at higher frequencies for $\theta = \pi/2$ were also seen by Yarom & Sharon (2014) and attributed to harmonics of the rotation rate.

3 DISCUSSION

In this study, we report the presence of inertial waves triggered by buoyant regions near the equator in a strongly time-dependant dynamo simulation. The low-frequency waves that are preferentially excited near the equator communicate the effects of the movement of buoyant anomalies to the vertical locations far from the equator. In principle, this is similar to the mechanism behind the 'trailing Taylor columns' observed in Hide's rotating tank experiments (Hide et al. 1968; Lighthill 1970) in that the columnar vortices 'follow' the buoyant anomalies as they drift. It may be noted that, for a nonmagnetic simulation at large Rayleigh number in a spherical shell, Glatzmaier & Olson (1993) suggested that equatorially-biased thermal plumes drive the columnar vortices that extend in the vertical direction, similar to Taylor columns produced by a moving sphere in a rotating fluid. Our results, (Figs. 4, 8, 9) provide statistical evidence in support of this suggestion, but for a dynamo simulation. These internally-driven, low-frequency inertial waves can help maintain the coherence of the columns. In particular, the columnarity associated with a rapidly evolving buoyancy field can be maintained if the buoyant anomalies continually emit low-frequency wave packets. These columns are, in turn, important for maintaining a dipolar magnetic field.
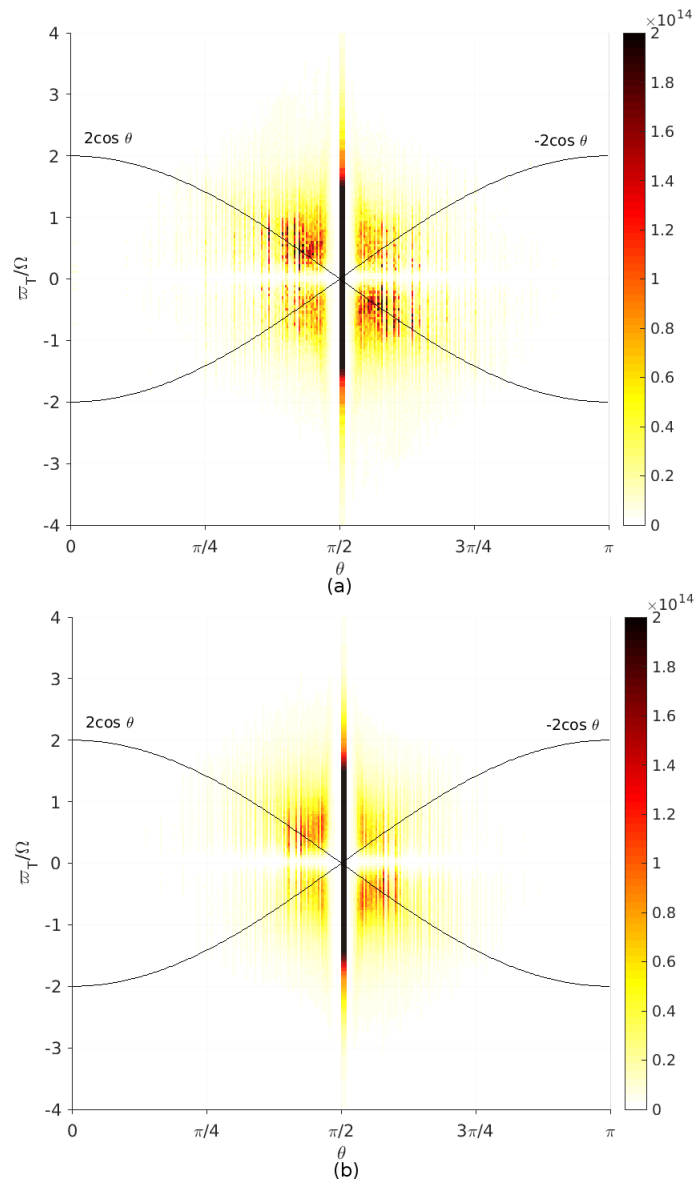
18   *Ranjan et al.*

Figure 11. (a) $E(\theta, \varpi_T)$ for the box $(0 \leq \phi/\pi \leq 0.25)$ (b) $E(\theta, \varpi_T)$ averaged over $0 \leq \phi/\pi \leq 2$. The white regions near $\theta = \pi/2$ are due to a relatively low resolution in θ there. In (a), the peak at $\theta = \pi/2$ occurs at $\varpi_T/\Omega = \pm 0.24$, and it is not visible due to lower plot threshold used to highlight off-axis waves.

We speculate that the results of this study will apply to the core since its Rayleigh number is expected to be very strongly supercritical (Gubbins 2001). On the other hand, internally-driven inertial waves are unlikely to be present at small values of Ra/Ra_{crit}, as evident from the application of our statistical techniques to a (non-magnetic) simulation at the onset of convection (Appendix B). The effect of decreasing the Ekman number, E, on the typical group speed of low-frequency inertial waves, $C_g \approx 2\Omega\delta$, is slightly harder to understand. In the dynamo simulations, which are mostly too viscous, a reduction in E usually leads to a reduction in δ, as is also expected from the viscous scaling,

$\delta = E^{1/3}d$ (King & Buffett 2013). Therefore, decreasing E will lead to lowering of the typical C_g values in simulations, which means larger travel-times of low-frequency inertial waves. However, in the core, the viscous scaling is not expected to hold and it is not known what sets the local length scale there. If the typical values of δ are in the range 1-10 km, the expected travel-times will be in the range $\sim$ 18-180 days.

Recent geomagnetic field models based on high resolution satellite data have revealed variation of Earth's core magnetic field on monthly time scales (Olsen & Mandea 2008). It may be tempting to speculate that these fast variations arise due to the arrival of inertial wave packets at the core-mantle boundary. However, geomagnetic data only allow to resolve dynamic features with the length scale of few hundred kilometers at best, and so a direct identification of inertial waves is unlikely. The results of their continuous action in maintaining geostrophy, however, may be identifiable. A geostrophic flow structure would imply an equatorially-symmetric flow at the core-mantle boundary, which seems compatible to a large degree with geomagnetic secular variation (Pais & Jault 2008; Gillet et al. 2011; Canet et al. 2014; Maffei & Jackson 2017). However, in this regard, it is important to note that the internally-driven inertial waves that are spontaneously triggered from buoyant anomalies (in Fig. 2b, for instance) should not be confused with boundary-driven quasi-geostrophic inertial modes (Zhang et al. 2001; Jault & Finlay 2015).

Perhaps it is important to note at this point that independent evidence (Bin Baqui et al. 2016; Sreenivasan & Davidson 2008; Davidson 2016) suggests that inertial waves cease to propagate when the small-scale Rossby number, $Ro_\delta = u/\Omega\delta_h$, exceeds a value of $0.2-0.6$ (depending on the precise definition). Consequently, our conclusion that the columnar structures are maintained by inertial waves implies that such structures will not be maintained when Ro_δ exceeds this threshold. It is interesting to note in this regard that for a suite of dynamo simulations (King et al. 2010), a loss of dipolarity is observed when the Ro_δ exceeds 0.1 (Roberts & King 2013; Oruba & Dormy 2014; Garcia et al. 2017). (Some researchers believe the geodynamo lies close to the dipolar-multipolar transition defined by $Ro_\delta = 0.1$ (Olson & Christensen 2006)). The corresponding Ro_δ in our simulation is 0.08, based on the definition in Christensen & Aubert (2006).

There is recent interest among the dynamo community regarding the dynamical role of waves in the core (Finlay et al. 2010; Jault & Finlay 2015). The fact that there could be a zoo of waves present in the core, possibly with overlapping frequencies, and that they co-exist with their source(s) makes their identification difficult. Nevertheless, our study suggests that the time-series of $\dot{u}_z$ is a good diagnostic to detect wave-fronts and that perhaps the methods used in this study can be extended to study other types of waves, such as the MAC waves (Buffett et al. 2016; Jaupart & Buffett 2017) wherein the role of the magnetic field and stratification are also important, torsional waves (Wicht & Christensen

20   *Ranjan et al.*

2010) or perhaps magnetic Rossby waves (Hori et al. 2017). An efficient planetary dynamo requires the azimuthally-averaged helicity to be of one sign in the north and another in the south. Inertial waves triggered near the equator are prime candidates for sustaining such an asymmetric helicity distribution (Davidson 2014). In this regard, the dynamical role of inertial waves in geodynamo simulations is being investigated and will be discussed in a subsequent study (Davidson & Ranjan 2017). Whether there are other vertically-propagating waves, such as the intermediate magnetic-Coriolis (MC) waves (Bardsley & Davidson 2016, 2017), which contribute to the creation of columnar structures in the simulations is still unclear. It is encouraging, however, that the frequency range displayed in Fig. 7 is close to that of inertial waves, and according to Bardsley & Davidson (2017) the properties of intermediate MC waves with such frequencies are similar to those of inertial waves.

ACKNOWLEDGMENTS

REFERENCES

Bardsley, O. P., & Davidson, P. A. 2016. Inertial-Alfvèn waves as columnar helices in planetary cores. *J. Fluid Mech. Rapids*, **805**.

Bardsley, O. P., & Davidson, P. A. 2017. The dispersion of magnetic–Coriolis waves in planetary cores. *Geophys. J. Int.*, **210(1)**, 18–26.

Bin Baqui, Y., Davidson, P. A., & Ranjan, A. 2016. Are there two regimes in strongly rotating turbulence?. *Phy. Fluids*, **28**, 045103.

Buffett, B., Knezek, N., & Holme, R. 2016. Evidence for MAC waves at the top of Earths core and implications for variations in length of day. *Geophys. J. Int.*, **204**, 1789–1800.

Busse, F. H. 1970. Thermal instabilities in rapidly rotating systems. *J. Fluid Mech.*, **44(3)**, 441–460.

Busse, F. H. 1975. A model of the geodynamo. *Geophys. J. Int.*, **42(2)**, 437-459.

Canet, E., Finlay, C. C., & Fournier, A. 2014. Hydromagnetic quasi-geostrophic modes in rapidly rotating planetary cores. *Phy. Earth Planetary Int.*, **229**, 1–15.

Christensen, U. R., & Aubert, J. 2006. Scaling properties of convection-driven dynamos in rotating spherical shells and application to planetary magnetic fields. *Geophys. J. Int.*, **166(1)**, 97–114.

Christensen, U.R., Aubert, J., & Hulot, G., 2010. Conditions for Earth-like geodynamo models. *Earth Planet. Sci. Lett.*, **296**, 487–496.

Christensen, U. R., & Wicht, J. 2015. Numerical dynamo simulations, in *Treatise on Geophysics (2nd ed.): Core dynamics (vol. 8)*, pp. 245–277, ed. Schubert, G.

Davidson, P. A. 2004. *Turbulence – an introduction for scientists and engineers. Oxford University Press*.

Davidson, P. A., Staplehurst, P. J., & Dalziel, S. B. 2006. On the evolution of eddies in a rapidly rotating system. *J. Fluid Mech.*, **557**, 135–144.

Davidson, P. A. 2013. *Turbulence in rotating, stratified and electrically conducting fluids*. Cambridge University Press.

Davidson, P. A. 2014. The dynamics and scaling laws of planetary dynamos driven by inertial waves. *Geophys. J. Int.*, **198(3)**, 1832–1847.

Davidson, P. A., & Ranjan, A. 2015. Planetary dynamos driven by helical waves-II. *Geophys. J. Int.*, **202**, 1646-1662.

Davidson, P. A. 2016. Dynamos driven by helical waves: scaling laws for numerical dynamos and for the planets. *Geophys. J. Int.*, **207(2)**, 680–690.

Davidson, P. A., & Ranjan, A. 2017. On the spatial segregation of helicity by inertial waves in dynamo simulations and planetary cores. *submitted to J. Fluid Mech.*.

Finlay, C. C., Dumberry, M., Chulliat, A., & Pais, M. A. 2010. Short timescale core dynamics: theory and observations. *Space Sci. Rev.*, **155(1-4)**, 177–218.

Garcia, F., Oruba, L., & Dormy, E. 2017. Equatorial symmetry breaking and the loss of dipolarity in rapidly rotating dynamos. *Geophys. Astro. Fluid Dyn.*, **111(5)**, 380–393.

Glatzmaier, G. A., & Olson, P. 1993. Highly supercritical thermal convection in a rotating spherical shell: centrifugal vs. radial gravity. *Geophys. Astro. Fluid Dyn.*, **70**, 113–136.

Glatzmaier, G. A. 2013. *Introduction to modeling convection in planets and stars*. Princeton university press

Gillet, N., Schaeffer, N., & Jault, D. 2011. Rationale and geophysical evidence for quasi-geostrophic rapid dynamics within the Earth's outer core. *Phys. Earth Planetary Int.*, **187(3)**, 380–390

Gizon, L., & Birch, A. C. 2005. Local helioseismology. *Living Reviews in Solar Physics*, **2(1)**, 1–131.

Greenspan, H. P. 1968. *The theory of rotating fluids*. Cambridge University Press.

Gubbins, D., & Bloxham, J. 1987. Morphology of the geomagnetic field and implications for the geodynamo. *Nature*, **325(6104)**, 509–511.

Gubbins, D. 2001. The Rayleigh number for convection in the Earth's core, *Phy. Earth Planetary Int.*. **128(1-4)**, 3–12.

Hide, R., Ibbetson, A., & Lighthill, M. J. 1968. On slow transverse flow past obstacles in a rapidly rotating fluid. *J. Fluid Mech.*. **32**, 251–272.

Holme, R. 2015. Large scale flow in the core, in *Treatise on Geophysics (2nd ed.): Core dynamics (vol. 8)*, pp. 91-113, ed. Schubert, G.

Hori, K., Teed, R. J., & Jones, C. A. 2017. The dynamics of magnetic Rossby waves in spherical dynamo simulations: A signature of strong-field dynamos?, *Phys. Earth Plan. Int.*, https://doi.org/10.1016/j.pepi.2017.07.008.

22   *Ranjan et al.*

Jault, D., & Finlay, C. C. 2015. Waves in the core and mechanical core–mantle interactions, in *Treatise on Geophysics (2nd ed.): Core dynamics (vol. 8)*, pp. 225-244, ed. Schubert, G.

Jaupart, E., & Buffett, B. 2017. Generation of MAC waves by convection in Earth's core. *Geophys. J. Int.*, **209(2)**, 1326–1336.

Kageyama, A., & Sato, T. 1997. Generation mechanism of a dipole field by a magnetohydrodynamic dynamo. *Phy. Rev. E*, **55(4)**, 4617–4626.

King, E. M., Soderlund, K. M., Christensen, U. R., Wicht, J., & Aurnou, J. M. 2010. Convective heat transfer in planetary dynamo models. *Geochem. Geophy. Geosys.* **11(6)**, Q06016.

King, E. M., & Buffett, B. A. 2013. Flow speeds and length scales in geodynamo models: The role of viscosity. *Earth Planetary Sci. Lett.*, **371**, 156–162.

Lighthill, M. J. 1970. The theory of trailing Taylor columns. *Proc. Camb. Phil. Soc.*. **68(02)**, 485–491.

Le Reun, T., Favier, B., Barker, A. J., & Le Bars, M. 2017. Inertial wave turbulence driven by elliptical instability. *Phys. Review Lett.*, **119(3)**, 034502.

Loper, D. E. 2001. On the structure of a Taylor column driven by a buoyant parcel in an unbounded rotating fluid. *J. Fluid Mech.*, **427**, 131–165.

Maffei, S., & Jackson, A. 2017. Kinematic validation of a quasi-geostrophic model for the fast dynamics in the Earth's outer core. *Geophys. J. Int.*, **210(3)**, 1772–1786.

Moffatt, H. K. 1970. Dynamo action associated with random inertial waves in a rotating conducting fluid.*J. Fluid Mech.*, **44(04)**, 705–719.

Olsen, N., & Mandea, M. 2008. Rapidly changing flows in the Earth's core. *Nature Geosc.*, **1**, 390–394.

Olson, P., Christensen, U. R., & Glatzmaier, G. A. 1999. Numerical modeling of the geodynamo: mechanisms of field generation and equilibration. *J. Geo. Res.*, **104(B5)**, 10383–10404.

Olson, P., & Christensen, U. R. 2006. Dipole moment scaling for convection-driven planetary dynamos. *Earth Planetary Sci. Lett.*, **250(3)**, 561–571.

Oruba, L., & Dormy, E. 2014. Transition between viscous dipolar and inertial multipolar dynamos. *Geophys. Res. Lett.*, **41(20)**, 7115–7120.

Pais, M. A., & Jault, D. 2008. Quasi-geostrophic flows responsible for the secular variation of the Earth's magnetic field. *Geophys. J. Int.*, **173(2)**, 421–443.

Ranjan, A., & Davidson, P. A. 2014. Evolution of a turbulent cloud under rotation. *J. Fluid Mech.*, **756**, 488–509.

Ranjan, A. 2017. Segregation of helicity in inertial wave packets. *Phy. Rev. Fluids*, **2(3)**, 033801.

Roberts, P. H., & King, E. M. 2013. On the genesis of the Earth's magnetism. *Rep. Prog. Phy.* **76(9)**, 096801.

Sakuraba, A., & Roberts, P. H. 2009. Generation of a strong magnetic field using uniform heat flux at the surface of the core. *Nature Geosc.*, **2**, 802–805.

Soderlund, K. M., King, E. M., & Aurnou, J. M. 2012. The influence of magnetic fields in planetary dynamo models. *Earth Planetary Sci. Lett.*, **333**, 9–20.

Schaeffer, N., Jault, D., Nataf, H-C., & Fournier, A. 2017. Turbulent geodynamo simulations: a leap towards

Earths core. *Geophys. J. Int.* **211**, 1–29.

Sreenivasan, B., & Davidson, P. A. 2008. On the formation of cyclones and anticyclones in a rotating fluid. *Phy. Fluids*, **20(8)**, 085104.

Taylor, G. I. 1921. Experiments on the motion of solid bodies in rotating fluids. *Proc. Roy. Soc. Lond. A*, **104**, 213–218.

Tilgner, A. 2000. Oscillatory shear layers in source driven flows in an unbounded rotating fluid. *Phy. Fluids*, **12(5)**, 1101–1111.

Wicht, J. 2002. Inner-core conductivity in numerical dynamo simulations. *Phy. Earth and Planetary Int.*, **132(4)**, 281–302.

Wicht, J. & Christensen, U. R. 2010. Torsional oscillations in dynamo simulations. *Geophys. J. Int.*, **181**, 1367–1380.

Yadav, R. K., Gastine, T., Christensen, U. R., Wolk, S. J., & Poppenhaeger, K. 2016. Approaching a realistic force balance in geodynamo simulations. *Proc. Nat. Acad. Sci.* **113(43)**, 12065–12070.

Yarom, E., & Sharon, E. 2014. Experimental observation of steady inertial wave turbulence in deep rotating flows. *Nature Physics*, **10(7)**, 510.

Zhang, K., & Busse, F. H. 1987. On the onset of convection in rotating spherical shells. **Geophys. Astro. Fluid Dyn.**, 39, 119–147.

Zhang, K., Earnshaw, P., Liao, X., & Busse, F. H. 2001. On inertial waves in a rotating fluid sphere. **J. Fluid Mech.**, 437, 103–119.

APPENDIX A: CO-ORDINATE TRANSFORM FROM SPHERICAL TO CYLINDRICAL POLAR

In MagIC, the velocity and magnetic field vectors are decomposed into toroidal and poloidal potentials (Christensen & Wicht 2015)

$$\boldsymbol{u}(r,\theta,\phi) = \nabla \times \nabla \times [\hat{\boldsymbol{e}}_r W(r,\theta,\phi)] + \nabla \times [\hat{\boldsymbol{e}}_r Z(r,\theta,\phi)] \tag{A.1}$$

$$\boldsymbol{B}(r,\theta,\phi) = \nabla \times \nabla \times [\hat{\boldsymbol{e}}_r g(r,\theta,\phi)] + \nabla \times [\hat{\boldsymbol{e}}_r h(r,\theta,\phi)],$$

where $W_l^m(r)$, $Z_l^m(r)$ are the poloidal and toroidal velocity potentials. The output from MagIC, which is in (l, m) (wavenumbers in meridional and azimuthal directions) space, is inverse-transformed to a cylindrical grid to get $\boldsymbol{u}, \boldsymbol{B}, T$ as a function of (s, ϕ, z) with $(N_s, N_\phi, N_z) = (81, 384, 246)$. The velocity components in spherical co-ordinates are (Glatzmaier 2013)

$$u_r = \frac{1}{r^2} \sum_{l,m} l(l+1) W_l^m Y_l^m \tag{A.2}$$

$$u_\theta = \frac{1}{r \sin\theta} \sum_{l,m} \left[\frac{\partial W_l^m}{\partial r} \sin\theta \frac{\partial Y_l^m}{\partial \theta} + Z_l^m \frac{\partial Y_l^m}{\partial \phi} \right] \tag{A.3}$$

24   *Ranjan et al.*

$$u_\phi = \frac{1}{r \sin\theta} \sum_{l,m} \left[\frac{\partial W_l^m}{\partial r} \frac{\partial Y_l^m}{\partial \phi} - Z_l^m \sin\theta \frac{\partial Y_l^m}{\partial \theta} \right] \tag{A.4}$$

where $Y_l^m(\theta, \phi) = P_l^m(\cos\theta)e^{im\phi}$, $P_l^m(\cos\theta)$ is Legendre Polynomial and $\sum_{l,m} = \sum_{l=0}^{l_{max}} \sum_{m=-l}^{l}$.
Using the spherical to cylindrical transformation matrix,

$$\begin{bmatrix} u_s \\ u_z \\ u_\phi \end{bmatrix} = \begin{bmatrix} \sin\theta & \cos\theta & 0 \\ \cos\theta & -\sin\theta & 0 \\ 0 & 0 & 1 \end{bmatrix} \begin{bmatrix} u_r \\ u_\theta \\ u_{\phi,} \end{bmatrix}$$

the s and z components of velocity may be obtained. The temperature perturbation

$$T(r, \theta, \phi) = \sum_{l,m} T_l^m(r) Y_l^m(\theta, \phi) \tag{A.5}$$

is transformed in the same way as u_r.

APPENDIX B: AZIMUTHALLY-DRIFTING MODES AT ONSET

A natural question that arises regarding the statistical techniques used in our study is: *are there any*
internally-driven inertial waves present at the onset of convection, and can they be detected using
the statistical techniques used in this study? To address this, we perform a (non-magnetic) simulation
of rotating convection in a spherical shell, using the MagIC code. The chosen parameters are $Ra =$
2.93×10^6 $(Ra/Ra_{crit} = 1.02)$, $E = 3 \times 10^{-5}$ and $Pr = 1$. The simulation is run for 1 viscous
diffusion time or 3.33×10^4 rotation units, and the output is transformed to cylindrical co-ordinates.
As predicted by theory (Busse 1970; Zhang & Busse 1987), the solution is the classical geostrophic
columnar structure, consisting of quasi-geostrophic modes. This is evident from Fig. A1 which shows
the equatorial slice of radial velocity, u_s, and for $s/d = 0.82$, $\phi - z$ slices of u_s and u_z, all at the same
time. It is interesting to note the familiar alternate cyclone-anticyclone structure in the $\phi - z$ slices, and
an asymmetry in the sign of u_z. Let us now repeat our statistical procedure of §2.1 for this simulation.
The resolution in space is $(74, 192, 148)$ points in (s, ϕ, z). We choose 300 time co-ordinates in the
duration $\Delta\Omega t = 10^4$, i.e. between $\Omega t = [2.33, 3.33] \times 10^4$. Note that the plots in Fig. A1 are at
$\Omega t = 2.33 \times 10^4$.

For $s/d = 0.82$, the longitude-time plots of $\partial T/\partial\phi$ at $z = 0$ (equator) and of $\dot{u}_z$ at $z/d = 0.65$
(above the equator) are shown in Figs. A2a,b respectively. Note that the columns drift in the prograde
or eastward direction, as would be expected at a small E (Zhang & Busse 1987). The slope in these
graphs indicates that the time taken for one complete rotation is ~ 7764 rotation units (0.233 diffusion
units), corresponding to a drift frequency of 9.4×10^{-9} sec^{-1} or 0.295 year^{-1}. In the vertical direction,
the flow is perfectly correlated at all times, as evident from Fig. A2c showing the cross-correlation
function, $R_{\phi-t}$ (14). The time-distance plot of $\dot{u}_z$, fixing $(s/d, \phi/\pi) = (0.82, 1)$, is shown in Fig. A3.
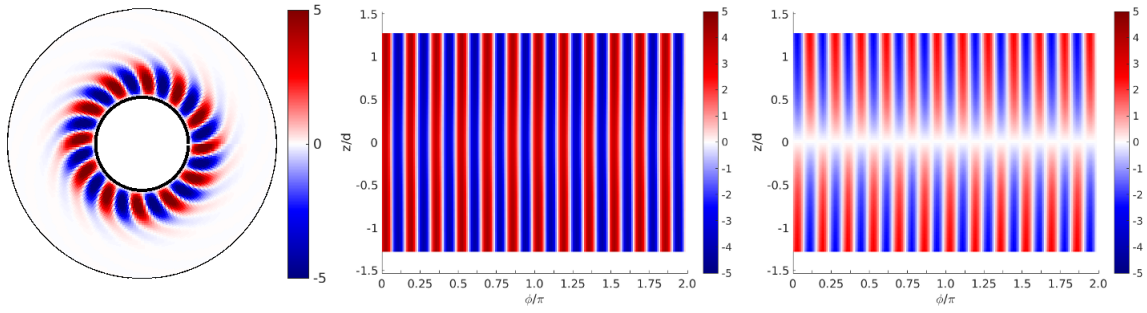
Figure A1. Onset calculation: equatorial slice of radial velocity, u_s, $\phi - z$ slices of u_s and u_z at $s/d = 0.82$.

Clearly, there are no internally-driven inertial waves present at the onset of convection and the only frequency present in the simulation is the drift frequency.
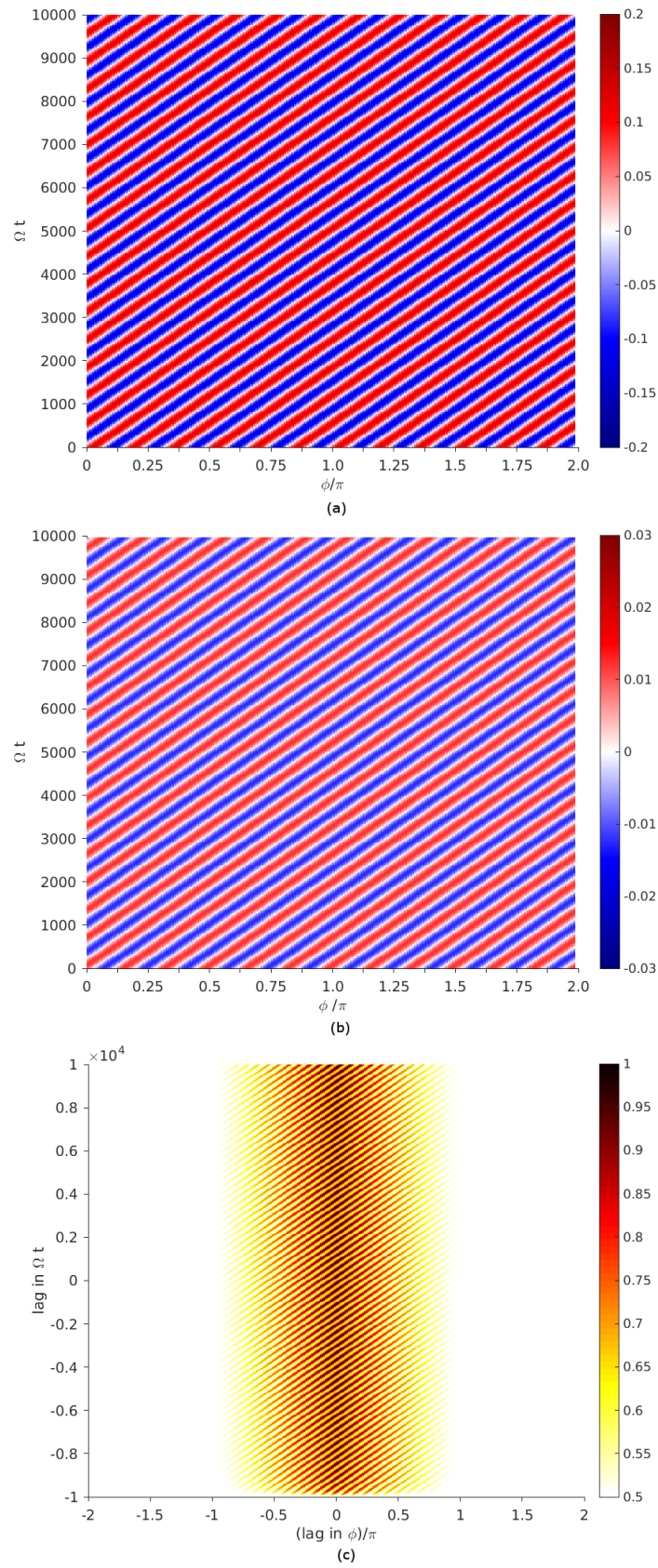
26   *Ranjan et al.*

Figure A2. Longitude-time plots of (a) $\partial T/\partial \phi$ at $z = 0$, (b) $\dot{u}_z$ at $z/d = 0.65$. (c) Cross-correlation, $R_{\phi-t}$ (14) of (a) with (b).
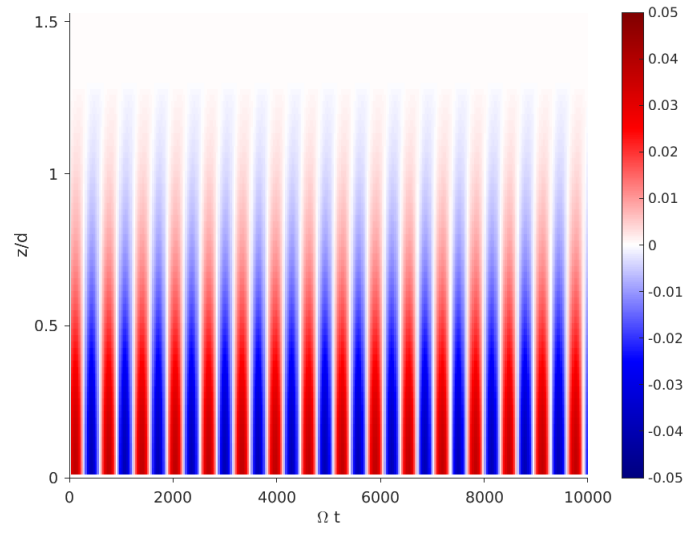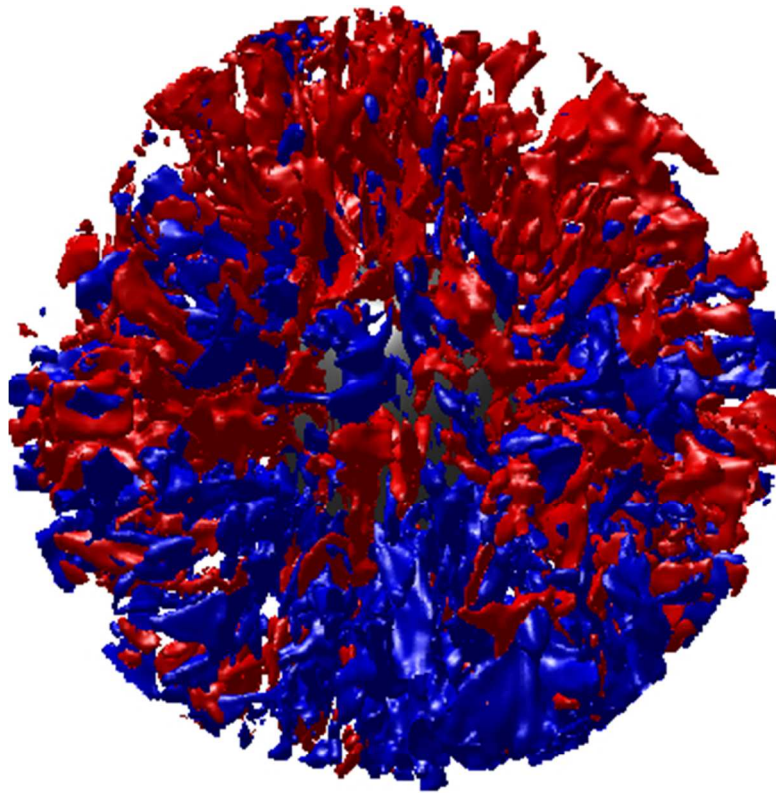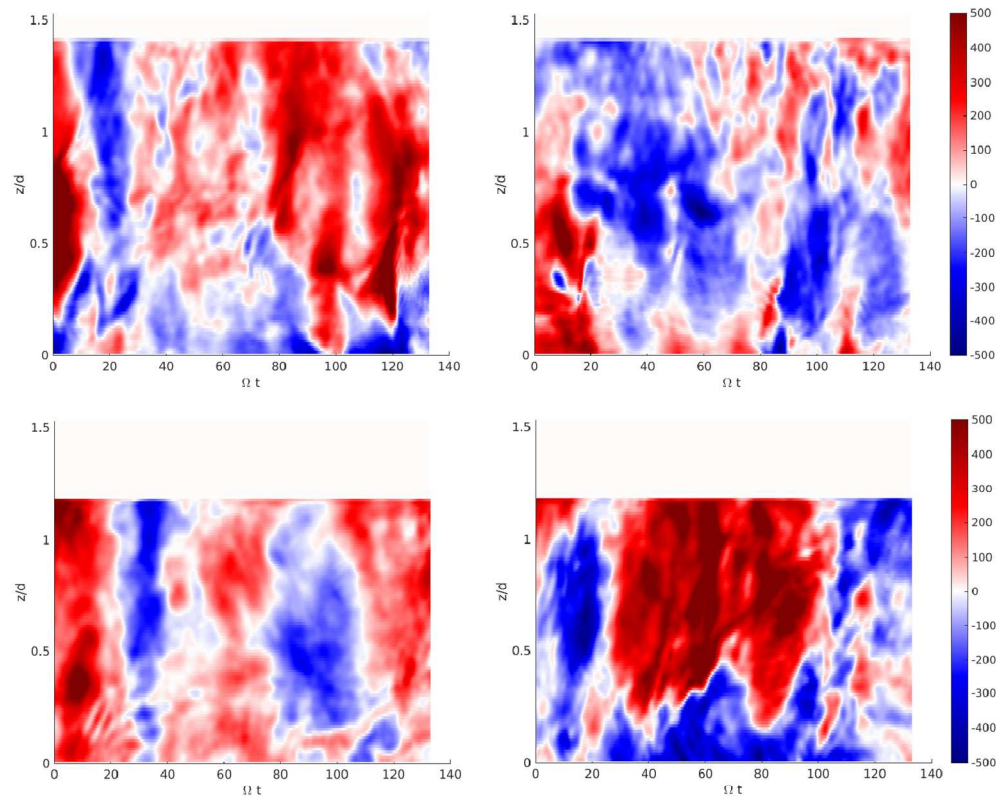
1
2
3
4
5
6
7
8
9
10
11
12
13
14
15
16
17
18
19
20
21
22
23
24
25
26
27
28
29
30
31
32
33
34
35
36
37
38
39
40
41
42
43
44
45
46
47
48
49
50
51
52
53
54
55
56
57
58
59
60

Figure A3. Time-distance plot of $\dot{u}_z$, for $(s/d, \phi/\pi) = (0.82, 1)$.

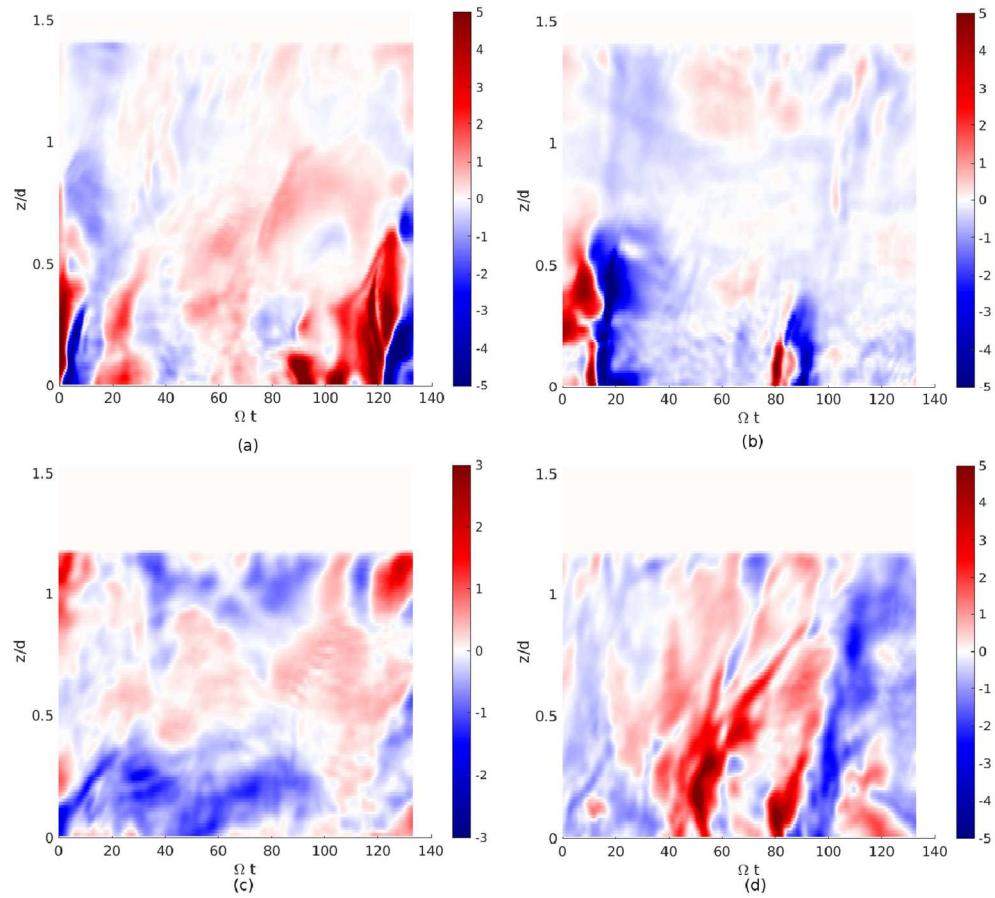Iso-surfaces of the radial component of the magnetic field. Red is positive, blue negative.

99x110mm (100 x 100 DPI)

Time-distance plots for vertical velocity

415x368mm (100 x 100 DPI)

Time-distance plots of the source, $\partial T/\partial\varphi$

399x388mm (100 x 100 DPI)